

# Enhanced enstrophy generation for turbulent convection in low-Prandtl-number fluids

Jörg Schumacher<sup>a,1</sup>, Paul Götzfried<sup>a</sup>, and Janet D. Scheel<sup>b</sup>

<sup>a</sup>Department of Mechanical Engineering, Technische Universität Ilmenau, D-98684 Ilmenau, Germany; and <sup>b</sup>Department of Physics, Occidental College, Los Angeles, CA 90041

Edited by Katepalli R. Sreenivasan, New York University, New York, NY, and approved June 23, 2015 (received for review March 13, 2015)

Turbulent convection is often present in liquids with a kinematic viscosity much smaller than the diffusivity of the temperature. Here we reveal why these convection flows obey a much stronger level of fluid turbulence than those in which kinematic viscosity and thermal diffusivity are the same; i.e., the Prandtl number  $Pr$  is unity. We compare turbulent convection in air at  $Pr = 0.7$  and in liquid mercury at  $Pr = 0.021$ . In this comparison the Prandtl number at constant Grashof number  $Gr$  is varied, rather than at constant Rayleigh number  $Ra$  as usually done. Our simulations demonstrate that the turbulent Kolmogorov-like cascade is extended both at the large- and small-scale ends with decreasing  $Pr$ . The kinetic energy injection into the flow takes place over the whole cascade range. In contrast to convection in air, the kinetic energy injection rate is particularly enhanced for liquid mercury for all scales larger than the characteristic width of thermal plumes. As a consequence, mean values and fluctuations of the local strain rates are increased, which in turn results in significantly enhanced enstrophy production by vortex stretching. The normalized distributions of enstrophy production in the bulk and the ratio of the principal strain rates are found to agree for both  $Pr$ s. Despite the different energy injection mechanisms, the principal strain rates also agree with those in homogeneous isotropic turbulence conducted at the same Reynolds numbers as for the convection flows. Our results have thus interesting implications for small-scale turbulence modeling of liquid metal convection in astrophysical and technological applications.

thermal convection | vorticity generation | direct numerical simulation | liquid metals

Turbulent convection depends strongly on the material properties of the working fluid that are quantified by the Prandtl number, the ratio of kinematic viscosity of the fluid to thermal diffusivity of the temperature,  $Pr = \nu/k$ . Compared with the vast number of investigations at  $Pr \geq 1$  (1, 2), the very-low- $Pr$  regime appears almost as a “terra incognita” despite many applications. Turbulent convection in the Sun is present at Prandtl numbers  $Pr < 10^{-3}$  (3–5). The Prandtl number in the liquid metal core of the Earth is  $Pr \sim 10^{-2}$  (6). Convection in material processing (7), nuclear engineering (8), or liquid metal batteries (9) has Prandtl numbers between  $3 \times 10^{-2}$  and  $10^{-3}$ . Rayleigh–Bénard convection (RBC), a fluid flow in a layer that is cooled from above and heated from below, is a paradigm for all of these examples. One reason for significantly fewer low- $Pr$  RBC studies is that laboratory measurements have to be conducted in opaque liquid metals such as mercury or gallium at  $Pr = 0.021$  (10–12). The lowest value for a Prandtl number that can be obtained in optically transparent fluids is  $Pr = 0.2$  for binary gas mixtures (13), i.e., an order of magnitude larger than in liquid metals. Direct numerical simulations (DNS) are currently the only way to gain access to the full 3D convective turbulent fields in low- $Pr$  convection (14–18). These simulations turn out to become very demanding if the small-scale structure of turbulence is to be studied, even for moderate Rayleigh number  $Ra$ , the parameter that quantifies the thermal driving in turbulent convection (19, 20). Whereas heat transport is reduced in low- $Pr$  convection, the production of vorticity and shear are enhanced significantly, which

amplifies the small-scale intermittency in these flows. An analysis of vorticity generation mechanisms in such flows and a comparison with other turbulent flows, which requires the resolution of spatial derivatives of the turbulent fields, is still missing. These details are, however, essential to improve parameterizations of the small-scale turbulence in low-Prandtl-number fluids such as algebraic heat flux and other subgrid-scale models (21, 22).

In the present work, we investigate the reasons for this enhanced vorticity generation in low- $Pr$  convection and compare and contrast the enstrophy production to turbulent convection at  $Pr \sim 1$ . Our studies are based on high-resolution 3D DNS. Rather than studying the  $Pr$  dependence of convection at a fixed Rayleigh number  $Ra$ , as is usually done, we compare two simulations at the same Grashof number  $Gr$ , which is defined by

$$Gr = \frac{g\alpha\Delta TH^3}{\nu^2} = \frac{Ra}{Pr}. \quad [1]$$

Here,  $g$  is the acceleration due to gravity,  $\alpha$  is the thermal expansion coefficient, and  $\Delta T$  is the total temperature difference across the cell height  $H$ . In such a comparison,  $Ra$  and  $Pr$  are varied now simultaneously and the corresponding dimensionless momentum equations (Eq. 4) remain unchanged. This implies that the strongly differing Prandtl numbers show up only in the advection–diffusion equation [5] for temperature. We demonstrate this perspective for two simulations at one Grashof number. We also mention that a similar discussion was emphasized in 2D quasi-geostrophic DNS (20). Fig. 1 illustrates our point of view. In Fig. 1 *A* and *C*, we show snapshots of temperature (Fig. 1 *A* and *C*, *Left*) and velocity magnitude (Fig. 1 *A* and *C*, *Right*) for the two runs. Compared with convection in air (Fig. 1 *A*), the temperature field in the liquid metal flow is much more diffusive,

## Significance

Low-Prandtl-number thermal convection flows in liquid metals for which the temperature diffusivity is much larger than the fluid viscosity have been studied much less frequently than convective flows in air or water, despite many important applications reaching from astrophysics to energy conversion. Currently, the turbulence in low-Prandtl-number flows is fully accessible only by three-dimensional simulations. Our numerical studies reveal why the small-scale turbulence is much more vigorous compared with convection in air. We also find that the generation of small-scale vorticity in the bulk of convection follows the same mechanisms and statistics as in idealized isotropic turbulence, especially for the low-Prandtl-number flow. This opens new perspectives for necessary turbulence parameterizations in applications.

Author contributions: J.S. and J.D.S. designed research; J.S., P.G., and J.D.S. performed research; J.S., P.G., and J.D.S. analyzed data; and J.S. and J.D.S. wrote the paper.

The authors declare no conflict of interest.

This article is a PNAS Direct Submission.

<sup>1</sup>To whom correspondence should be addressed. Email: joerg.schumacher@tu-ilmenau.de.

This article contains supporting information online at [www.pnas.org/lookup/suppl/doi:10.1073/pnas.150511112/-DCSupplemental](http://www.pnas.org/lookup/suppl/doi:10.1073/pnas.150511112/-DCSupplemental).



**Table 1. Summary of turbulent convection (RB) and homogeneous isotropic (HI) box turbulence runs**

Run	Ra	Pr	Gr	$N_{BL}$	$N^3$	Re	Nu	$\eta_K/(10^{-3}H)$	$L_B/H$	$\delta_T/H$
RB1	$3.33 \times 10^8$	0.7	$4.76 \times 10^8$	40	$1.51 \times 10^9$	$3,720 \pm 60$	$44.9 \pm 1.2$	$2.41 \pm 0.01$	$0.052 \pm 0.001$	0.011
RB2	$10^7$	0.021	$4.76 \times 10^8$	26	$1.51 \times 10^9$	$8,450 \pm 100$	$10.1 \pm 0.3$	$1.48 \pm 0.01$	$0.13 \pm 0.01$	0.049
HI1	—	—	—	—	$512^3$	$3,760 \pm 30$	—	$2.15 \pm 0.02$	—	—
HI2	—	—	—	—	$512^3$	$8,650 \pm 40$	—	$1.17 \pm 0.01$	—	—

The number of grid planes inside the velocity boundary layer is denoted as  $N_{BL}$ . The number  $N^3$  for RB1 and RB2 is obtained as  $N^3 = N_e \times N_p^3$ , with  $N_e$  being the total number of spectral elements and  $N_p - 1$  being the order of the Lagrangian interpolation polynomial in each space direction. The Reynolds number is  $Re = u_{rms}H/\nu$  and the Nusselt number is  $Nu = 1 + (Ra Pr)^{1/2} \langle wT \rangle_{V,t}$ . The Kolmogorov and Bolgiano lengths follow from [6] and thermal boundary layer thickness from [2].

We observe in Fig. 2A that both scales depend sensitively on the averaging volume and Prandtl number. In all subvolumes, the Bolgiano scales of the low-Pr run RB2 exceed the ones of RB1. In contrast, the Kolmogorov scales are always smaller in run RB2 than in RB1. The ratio of both scales that is shown in Fig. 2B is about a factor of 2 larger in RB2 than in RB1, which means that the cascade range grows as Pr decreases. The strong drop of  $L_B$  for  $V$  and  $Pr=0.7$  in Fig. 2A is due to the strong enhancement of  $\epsilon_T$  in the thinner thermal boundary layer.

Another length that is used in low-Pr convection is the Corrsin scale, which is at a fixed ratio to the Kolmogorov scale,  $\eta_C = \eta_K Pr^{-3/4}$ . Simulations in slab geometry with periodic side walls revealed a Kolmogorov 5/3 scaling of spectra above wavenumbers  $\eta_C^{-1}$  (29). They suggest a Kolmogorov cascade below  $\eta_C$  rather than  $L_B > \eta_C$  in low-Pr convection. In Fig. 2A, we find that  $\eta_{C,j}$  falls consistently between  $\eta_{K,j}$  and  $L_{B,j}$  in all subvolumes for  $Pr=0.021$ . For  $Pr=0.7$ ,  $\eta_{C,j}$  is very close to  $\eta_{K,j}$  so we did not plot it.

We see furthermore in Fig. 2C that the mean energy dissipation rate,  $\epsilon_j$  is enhanced in all subvolumes for RB2, which is the reason for the smaller Kolmogorov scales  $\eta_{K,j}$ . Whereas the root-mean-square (rms) value of the temperature,  $T_{rms,j}$ , remains nearly unchanged, both in the subvolumes and with respect to Pr, significant differences are found for the root-mean-square value

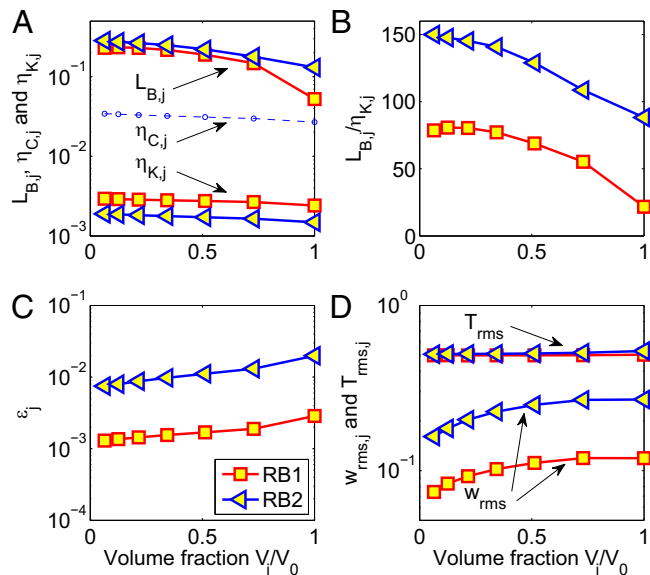


**Fig. 2.** (A–D) Statistical analysis in subvolumes of the cell. Triangles are for RB2 and squares for RB1. (A) Bolgiano and Kolmogorov scales as a function of the volume fraction  $V_j/V$ . Additionally, we plot the Corrsin length  $\eta_{C,j} = \eta_{K,j} Pr^{-3/4}$  for RB2. (B) Ratio of both scales. (C) Mean kinetic energy dissipation rates. (D) Root-mean-square value of temperature  $T$  and vertical velocity  $u_z (=w)$ . The exact size of the subvolumes  $V_j$  is listed in *SI Text*.

of the vertical velocity,  $w_{rms,j}$ , as seen in Fig. 2D. All rms values of RB2 exceed those of RB1 by a factor of 3. As a consequence, the Reynolds number grows from  $Re = 3,760 \pm 30$  for RB1 to  $Re = 8,650 \pm 40$  for RB2.

It has been emphasized in ref. 27 that the Kolmogorov-like cascade  $\eta_K \ll \ell \ll L_B$  in convection differs slightly from the one in classical fluid turbulence. The main mechanism of kinetic energy injection is provided by the thermal plumes that have a characteristic stem width of the size of the thermal boundary layer thickness  $\delta_T$ . These plumes get broader due to thermal diffusion while they rise (or fall) and thus inject kinetic energy dominantly for scales  $\ell > \delta_T$ . The kinetic energy injection and the resulting enhancement of the vertical velocity fluctuations are consequently inspected best by a combined scale-resolved analysis of vertical velocity and temperature increments. In this way, sweeping effects by the large-scale circulation in the closed cell are also removed. The increments are defined as

$$\Delta_r w(r_m) = w(x_m + r_m) - w(x_m), \quad [8]$$

$$\Delta_r T(r_m) = T(x_m + r_m) - T(x_m), \quad [9]$$

where  $r_m = r_{||}$ , i.e., parallel to the direction of the acceleration of gravity, or perpendicular,  $r_m = r_{\perp}$ . In *SI Text*, we derive the equation for the spatial correlations of the vertical velocity component,  $R_{zz}(r_m) = \langle w(x_m)w(x_m + r_m) \rangle$ , with  $\langle \cdot \rangle$  denoting a spatiotemporal average (30). The only scale-dependent source term in this equation is the mixed-increment moment  $S_{wT}(r) = \langle \Delta_r w \Delta_r T \rangle$ . This is plotted in Fig. 3A vs. the distance  $r/\delta_T$  for subvolume  $V_1$  (see *SI Text* for analysis in other subvolumes).  $S_{wT}$  is determined in both  $x$  and  $y$  vertical planes through the center of the cell for  $r_{||}$  and  $r_{\perp}$ . Close to the Kolmogorov scale, the flow is spatially smooth such that  $S_{wT}(r) \sim r^2$  follows as expected for small  $r$ . Kolmogorov and Bolgiano scales are indicated. It can be seen that the mixed-increment moment for RB2 is larger than for RB1. This holds over the whole Kolmogorov-like range, which is indicated by double-headed arrows in Fig. 3. A larger amount of kinetic energy is thus injected in RB2 compared with RB1, which is in line with larger mean energy dissipation rates  $\epsilon_j$  from Fig. 2C. Our finding is robust when the analysis is repeated in other subvolumes  $V_j$  (*SI Text*). We also observe that the increments with respect to  $r_{\perp}$  are always larger in both datasets than those with  $r_{||}$ . Fig. 3B, *Inset* explains this observation by a rising plume and the corresponding distances. Such a rise is always accompanied by recirculations outside the stem due to incompressibility (see Fig. 5F).

In Fig. 3B, we show the correlation coefficient

$$C(r) = \frac{\langle \Delta_r w \Delta_r T \rangle}{\sqrt{\langle (\Delta_r w)^2 \rangle \langle (\Delta_r T)^2 \rangle}}, \quad r = \{r_{||}, r_{\perp}\}, \quad [10]$$

with  $-1 \leq C(r) \leq 1$ . The variation of  $C(r_{\perp})$  of RB2 is particularly large across the range  $\eta_K \leq \ell \leq L_B$  and peaks for scales  $\ell > \delta_T$ . This

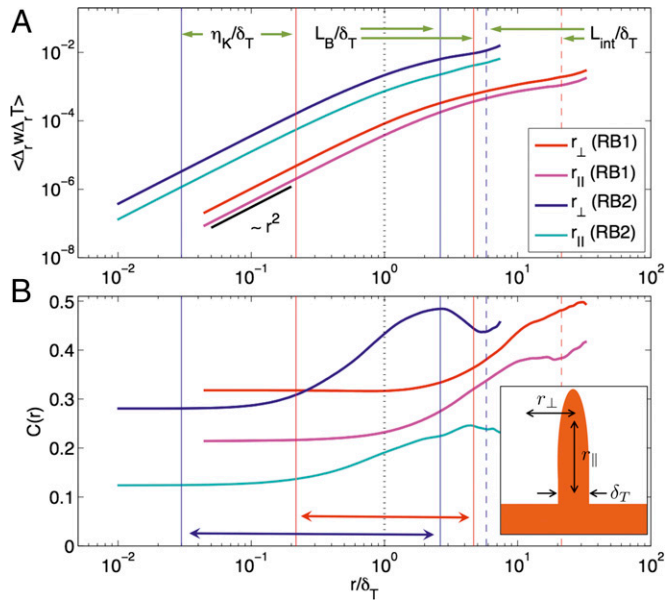


**Fig. 3.** (A) Time-averaged mixed-increment moment  $\langle \Delta_r w \Delta_r T \rangle$  as a function of  $r/\delta_T$ , where  $\delta_T$  is the thermal boundary layer thickness. Also plotted are scales  $\eta_K$  and  $L_B$  and the integral length scale  $L_{int} = 1/\langle w^2 \rangle \int \langle w(z+r_z)w(z) \rangle dr_z$ . They are indicated as vertical lines, red for RB1 and blue for RB2. (B) Correlation coefficient  $C(r)$  as given in Eq. 10. The horizontal double-headed arrows indicate the extension of the Kolmogorov-like cascade range, red for RB1 and blue for RB2. All data are obtained in  $V_1$ .

implies that the majority of kinetic energy is injected in the range  $r > \delta_T$ , i.e., at the larger scales, and that the low-Prandtl flow is thus closer to the classical Kolmogorov turbulence, at least for  $\ell \lesssim \delta_T$ . Our findings are also consistent with a recent spectral analysis conducted in ref. 31. Although for  $Pr = 1$ , Kumar et al. (31) showed that the spectral energy flux did not decrease for scales below the buoyancy-dominated scale  $\eta_C$ . For RB2, we get  $\eta_C \approx 0.6\delta_T$  (Fig. 3B).

### Strain Rate Distribution and Entropy Production

How is this stronger turbulence cascade manifested in the small-scale gradient statistics? As a first step, we investigate the distribution of the principal strain rates  $\alpha > \beta > \gamma$  with  $\alpha + \beta + \gamma = 0$ , the eigenvalues of the rate of strain tensor  $S_{ij} = (\partial_j u_i + \partial_i u_j)/2$ . In Fig. 4A and C, we show the probability density functions (PDFs) of the principal strain rates for RB1 and RB2 in one of the bulk volumes,  $V_4$ , and compare the results with homogeneous isotropic box turbulence runs, HI1 and HI2, in Fig. 4B and D for the corresponding Reynolds numbers. The strain rates are given in units of an inverse large-scale eddy turnover time in both flows to make them comparable. Convection data are obtained from 84 and 206 statistically independent snapshots for RB1 at  $Pr = 0.7$  and RB2 at  $Pr = 0.021$ , respectively. The tails of all three PDFs of RB2 are much more extended than those of RB1, which implies an enhanced local shear rate. Both sets of PDFs, RB1 and HI1 as well as RB2 and HI2, almost coincide. In SI Text, we list the mean principal components for all subvolumes  $V_j$  in RB1 and RB2 and their ratios together with the data for HI1 and HI2. The ratio of the principal rates is almost unchanged at about  $\langle \alpha \rangle : \langle \beta \rangle : \langle \gamma \rangle = 4.3 \pm 0.1 : 1 : -5.3 \pm 0.1$  in all cases, except when the wall regions, i.e., regions with the largest shear rates in the convection cell, are included. Furthermore, the ratio is similar to that in other flows (32, 33). The strongly stretched tails of the strain rate PDFs reflect the enhanced small-scale intermittency of fluid turbulence in RB2. Although the amplitudes differ, the

ratio of the mean principal strain rates agrees, which suggests qualitatively similar small-scale statistical properties.

We derive the transport equation for the vorticity  $\omega_i = \epsilon_{ijk} \partial_j u_k$  from [4] to obtain the balance for the local enstrophy,  $\Omega(\mathbf{x}, t) = \omega^2/2$ :

$$\frac{d\Omega}{dt} = \omega_i S_{ij} \omega_j + \epsilon_{3jk} \omega_j \frac{\partial T}{\partial x_k} + \frac{1}{2\sqrt{Gr}} \frac{\partial^2 (\omega_i^2)}{\partial x_k^2} - \epsilon_{\omega}. \quad [11]$$

The four terms on the right-hand side denote enstrophy production due to vortex stretching,  $P_v = \omega_i S_{ij} \omega_j$ ; enstrophy production due to the temperature gradient,  $P_T = \epsilon_{3jk} \omega_j \partial_k T$ ; and two terms,  $D$  and  $\epsilon_{\omega}$ . The last term is the enstrophy dissipation rate  $\epsilon_{\omega} = 1/\sqrt{Gr} (\partial_k \omega_i)^2 > 0$ . Because the flow is in a statistically stationary state, all four terms on the right-hand side add up to zero when averaging over  $V$  and time (Table 2). With decreasing Prandtl number the ratio  $\langle P_v \rangle / \langle P_T \rangle$  grows significantly in the whole cell and even stronger in the bulk volume. This shows that  $P_v$  becomes the sole relevant enstrophy generation mechanism for RB2 and in the bulk, similar to classical Kolmogorov turbulence.

The PDFs of  $P_v$  are displayed in Fig. 5A and C. All are strongly skewed to positive amplitudes, implying a net enstrophy production by vortex stretching, similar to that in ref. 34. In Fig. 5A we observe for RB1 that the positive tail is slightly more extended when the data are taken in  $V_4$  rather than in  $V$  (SI Text). A similar, but more enhanced difference between  $V$  and  $V_4$  is seen in Fig. 5C, which is for RB2. Fig. 5A and C shows also that the distributions in the bulk volume collapse very well with those obtained for HI1 and HI2, respectively. We also find that the ratio of the rms values of the enstrophy production by vortex stretching,  $P_{v,rms}(V)/P_{v,rms}(V_4)$ , increases from three in RB1 to five in RB2. We conclude that the vortex stretching is significantly enhanced in boundaries for both Prandtl numbers. Fig. 5E provides further support for the strongly enhanced small-scale turbulence in RB2 by monitoring the time evolution of  $P_{v,rms}(V)$  in both convection runs.

We proceed with the analysis by taking an average of the terms in Eq. 11 over the whole-cell cross-section  $A$  and time at a fixed

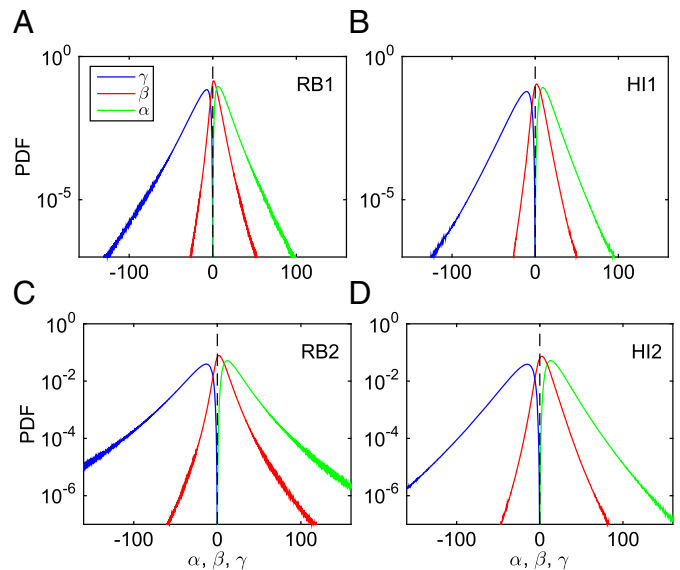


**Fig. 4.** (A–D) Probability density functions of the principal rates of strain for the four flows. In all four runs the principal rates are given in units of the inverse large-scale eddy turnover time  $T_L^{-1} = \langle \epsilon \rangle / k^2$  with  $k^2$  being the turbulent kinetic energy  $k^2 = \langle u_i^2 \rangle / 2$ . The mean values in the convection cases are determined over the volume  $V_4$  and with respect to time. (A) Run RB1; (B) Run HI1; (C) Run RB2; (D) Run HI2.

**Table 2. Time- and volume-averaged terms of the enstrophy balance [11]**

Quantity	RB1 in $V$	RB2 in $V$	RB1 in $V_4$	RB2 in $V_4$
$\langle P_v \rangle$	$58.4 \pm 0.7$	$1,186 \pm 11$	$30.5 \pm 1.5$	$484 \pm 16$
$\langle P_T \rangle$	$4.38 \pm 0.06$	$5.81 \pm 0.03$	$1.33 \pm 0.08$	$1.20 \pm 0.05$
$\langle D \rangle$	$27.6 \pm 0.5$	$351 \pm 4$	—	—
$-\langle \epsilon_\omega \rangle$	$-90 \pm 1$	$-1,541 \pm 14$	$-33.3 \pm 1.5$	$-503 \pm 16$
Sum	$0 \pm 1.4$	$1.4 \pm 18$	—	—
$\langle P_v \rangle / \langle P_T \rangle$	$13.3 \pm 0.2$	$204 \pm 2$	$23 \pm 1.8$	$403 \pm 20$
$\langle \Omega^2 \rangle$	$62.5 \pm 0.5$	$434 \pm 2$	$32.0 \pm 1.1$	$195 \pm 3$

For averages over  $V$  all source terms sum up to zero. For averages over the bulk subvolume  $V_4$  additional fluxes result. All source terms are given in units  $(U_f/H)^3$ . The error is given by the SD of the mean.

height  $z$  as in ref. 36. The two time-averaged terms that we denote by  $\langle P_v(z) \rangle$  and  $\langle P_T(z) \rangle$  are displayed in the vicinity of the heating plate in Fig. 5 *B* and *D*. First, we can see that  $\langle P_v \rangle \gg \langle P_T \rangle$  for all  $z$  and that in agreement with our previous observations on

strain rates,  $\langle P_v(\text{RB2}) \rangle \gg \langle P_v(\text{RB1}) \rangle$ . Second,  $\langle P_T \rangle < 0$  in the vicinity of the walls for both cases. Production by vortex stretching obeys a maximum inside the viscous boundary layers for both and remains nearly unchanged in the rest of the cell.

The maximum of  $\langle P_v \rangle$  roughly coincides with a minimum in  $\langle P_T \rangle$  as seen in Fig. 5 *B* and *D*. This connection is conceptualized by the sketch for a simple one-dimensional case in Fig. 5*F*. Inside the viscous boundary layer shearing motion dominates and lumps together segments of the thermal boundary layer into (sheet-like) plumes. On the one hand, such a shear flow generates enstrophy and thus causes the maximum of  $\langle P_v \rangle$ . On the other hand, it causes  $\langle P_T \rangle < 0$  because shear motion converges toward the stem of the plume. This means that enstrophy is consumed for the plume detachment. For a simple near-wall flow  $u_y = |S|z$ , it follows that  $\omega_x = -|S| < 0$  and thus  $P_T = \omega_x \partial_y T < 0$  because  $\partial_y T > 0$ . For  $z > \lambda_v$  the plume rises into the bulk, which is accompanied by a strong vertical upwelling. Due to the incompressibility of the flow, fluid is sucked in next to the rising plume. Thus,  $\omega_x > 0$  and consequently a positive enstrophy production occurs due to the temperature gradient.

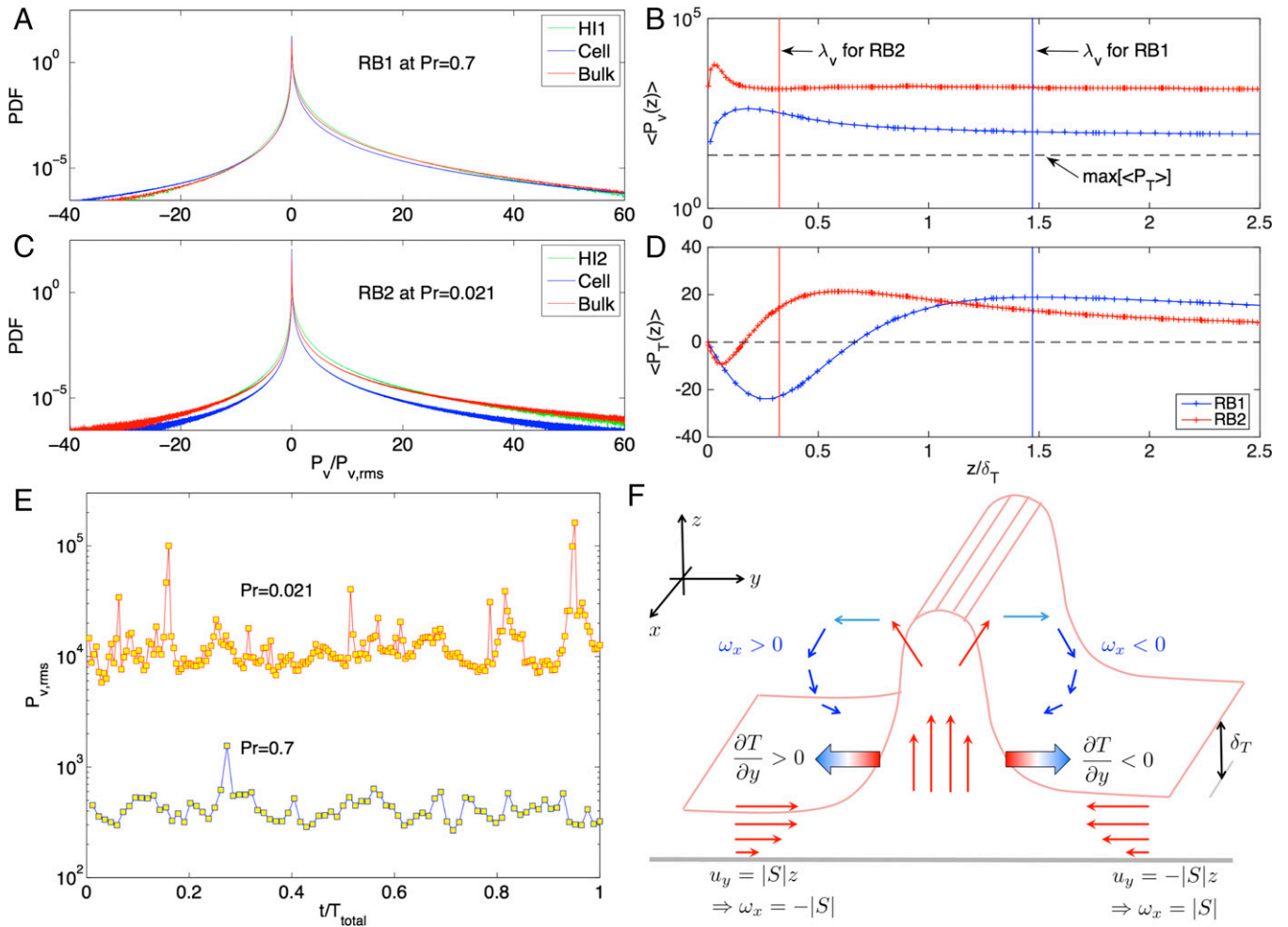


**Fig. 5.** Enstrophy production for different Prandtl number flows. (A and C) Normalized probability density function (PDF) of the production due to vortex stretching,  $P_v = \omega_i S_{ij} \omega_j$ . We compare data for the full volume (denoted cell) and a subvolume in the bulk of the cell (denoted bulk, which equals  $V_4$ ). For comparison we also display the PDFs of the corresponding isotropic box turbulence runs. (B and D) Plane-time averaged vertical profiles of the enstrophy production due to vortex stretching  $\langle P_v(z) \rangle$  (B) and due to the temperature gradient  $\langle P_T(z) \rangle$  (D) in the vicinity of the heating plate. The production term  $\langle P_T(z) \rangle$  is negative in the vicinity of the walls for both cases. The distance from the wall is given in units of the corresponding thermal boundary layer thickness  $\delta_T$ . The viscous boundary layer thicknesses  $\lambda_v$  are evaluated from slopes of gradients at the isothermal walls (35) and indicated by solid vertical lines. The dashed line in B shows the global maximum of  $\langle P_T(z) \rangle$  for the low-Pr run. (E) Root-mean-square values of  $P_v$  obtained for the whole cell as a function of the time that is normalized with respect to the total integration time. (F) The sketch explains the connection between enstrophy consumption,  $P_T < 0$ , and the detachment of a line-like plume in a simple one-dimensional picture.

## Summary and Discussion

We have presented a high-resolution simulation study that reveals the enhanced enstrophy generation mechanisms in turbulent convection at very low Prandtl numbers. Our high-resolution DNS demonstrate that the Kolmogorov-like cascade range grows because the Bolgiano scale  $L_B$  increases and the Kolmogorov scale  $\eta_K$  decreases as Pr gets smaller for the same Gr. In parallel, the flux of kinetic energy down to the smaller scales, which is given by the mean energy dissipation rate, is enhanced. By means of the mixed temperature–velocity structure function, we show that kinetic energy is injected into the convection flow on all scales  $\eta_k \leq \ell \leq L_B$ . The amount of injected energy is systematically larger for the low-Prandtl-number case and dominates starting from the thermal boundary layer thickness scale  $\delta_T$  that is also equal to the average width of the thermal plumes. The resulting more vigorous fluid turbulence is manifested by a larger-flow Reynolds number that enhances the amplitudes of the local strain and thus the enstrophy generation, dominantly due to vortex stretching. Despite the different driving of the fluid turbulence via the coupling to the temperature over a whole range of scales and the reduced number of statistically homogeneous directions, the normalized PDFs of enstrophy production and the ratio of the principal strain rates—two typical measures of

the small-scale velocity gradient statistics—are found to agree with the idealized classical Kolmogorov turbulence.

Our study provides thus further numerical evidence for the universality of small-scale turbulence as, for example, discussed recently in ref. 37. This opens interesting perspectives for the modeling of small-scale turbulent statistics that is necessary for several important applications of low-Prandtl-number convection. Simulations at higher Rayleigh and/or lower Prandtl numbers will obtain a sufficient scale separation to identify either the Corrsin or the Bolgiano scale as the large scale of a Kolmogorov-like cascade in low-Pr convection. A further point for future work is to study how this enhanced fluid turbulence couples back to the boundary layer dynamics.

**ACKNOWLEDGMENTS.** Helpful discussions with J. Aurnou and G. Grätzbach are acknowledged. This work is supported by Research Unit 1182 and Research Training Group 1567 of the Deutsche Forschungsgemeinschaft. We acknowledge supercomputing time at the Jülich Supercomputing Centre provided by Grants HIL07 and HIL08 of the John von Neumann Institute for Computing. Furthermore, we acknowledge an award of computer time provided by the Innovative and Novel Computational Impact on Theory and Experiment (INCITE) program. This research used resources of the Argonne Leadership Computing Facility at the Argonne National Laboratory, which is supported by the US Department of Energy under Contract DE-AC02-06CH11357. J.S. thanks the Institute of Pure and Applied Mathematics at University of California, Los Angeles, and the US National Science Foundation for financial support.

- Kadanoff LP (2001) Turbulent heat flow: Structures and scaling. *Phys Today* 54(8):34–39.
- Chillà F, Schumacher J (2012) New perspectives in turbulent Rayleigh-Bénard convection. *Eur J Phys E* 35:58.
- Christensen-Dalsgaard J, Gough DO, Thompson MJ (1991) The depth of the solar convection zone. *Astrophys J* 378:413–437.
- Sreenivasan KR, Donnelly RJ (2001) Role of cryogenic helium in classical fluid dynamics: Basic research and model testing. *Adv Appl Mech* 37:239–276.
- Hanasoge SM, Duvall TL, Jr, Sreenivasan KR (2012) Anomalous weak solar convection. *Proc Natl Acad Sci USA* 109(30):11928–11932.
- King EM, Aurnou JM (2013) Turbulent convection in liquid metal with and without rotation. *Proc Natl Acad Sci USA* 110(17):6688–6693.
- Asai S (2012) *Electromagnetic Processing of Materials: Materials Processing by Using Electric and Magnetic Functions* (Springer, Heidelberg).
- Grätzbach G (2013) Challenges in low-Prandtl number heat transfer simulation and modelling. *Nucl Eng Des* 264:41–55.
- Kelley DH, Sadoway DR (2014) Mixing in a liquid metal electrode. *Phys Fluids* 26:057102.
- Takeshita T, Segawa T, Glazier JA, Sano M (1996) Thermal turbulence in mercury. *Phys Rev Lett* 76(9):1465–1468.
- Cioni S, Ciliberto S, Sommeria J (1997) Strongly turbulent Rayleigh-Bénard convection in mercury: Comparison with results at moderate Prandtl number. *J Fluid Mech* 335:111–140.
- Büttner L, et al. (2013) Dual-plane ultrasound flow measurements in liquid metals. *Meas Sci Technol* 24:055302.
- Liu L, Ahlers G (1997) Rayleigh-Bénard convection in binary gas mixtures: Thermophysical properties and the onset of convection. *Phys Rev E Stat Phys Plasmas Fluids Relat Interdiscip Topics* 55:6950–6968.
- Camussi R, Verzicco R (1998) Convective turbulence in mercury: Scaling laws and spectra. *Phys Fluids* 10:516–527.
- Kerr RM, Herring JR (2000) Prandtl number dependence of Nusselt number in direct numerical simulations. *J Fluid Mech* 419:325–344.
- Silano G, Verzicco R, Sreenivasan KR (2010) Numerical simulations of Rayleigh-Bénard convection for Prandtl numbers between  $10^{-1}$  and  $10^4$  and Rayleigh numbers between  $10^5$  and  $10^9$ . *J Fluid Mech* 662:409–446.
- Verma MK, Mishra PK, Pandey A, Paul S (2012) Scalings of field correlations and heat transport in turbulent convection. *Phys Rev E Stat Nonlin Soft Matter Phys* 85(1 Pt 2):016310.
- van der Poel EP, Stevens RAJM, Lohse D (2013) Comparison between two- and three-dimensional Rayleigh-Bénard convection. *J Fluid Mech* 736:177–194.
- Breuer M, Wessling S, Schmalzl J, Hansen U (2004) Effect of inertia in Rayleigh-Bénard convection. *Phys Rev E Stat Nonlin Soft Matter Phys* 69(2 Pt 2):026302.
- Calkins MA, Aurnou JM, Eldredge JD, Julien K (2012) The influence of fluid properties on the morphology of core turbulence and the geomagnetic field. *Earth Planet Sci Lett* 359–360:55–60.
- Gizon L, Birch AC (2012) Helioseismology challenges models of solar convection. *Proc Natl Acad Sci USA* 109(30):11896–11897.
- Shams A, Roelofs F, Baglietto E, Lardeau S, Kenjeres S (2014) Assessment and calibration of an algebraic turbulent heat flux model for low-Prandtl fluids. *Int J Heat Mass Transfer* 79:589–601.
- Fischer PF (1997) An overlapping Schwarz method for Spectral Element Solution of the incompressible Navier-Stokes equations. *J Comput Phys* 133:84–101.
- Deville MO, Fischer PF, Mund EH (2002) *High-Order Methods for Incompressible Fluid Flow* (Cambridge Univ Press, Cambridge, UK).
- Scheel JD, Emran MS, Schumacher J (2013) Resolving the fine-scale structure in turbulent Rayleigh-Bénard convection. *New J Phys* 15:113063.
- Schumacher J, Sreenivasan KR, Yakhot V (2007) Asymptotic exponents from low-Reynolds-number flows. *New J Phys* 9:89.
- Lohse D, Xia K-Q (2010) Small-scale properties of turbulent Rayleigh-Bénard convection. *Annu Rev Fluid Mech* 42:335–364.
- Kaczorowski M, Xia K-Q (2013) Turbulent flow in the bulk of Rayleigh-Bénard convection: Small-scale properties in a cubic cell. *J Fluid Mech* 722:596–617.
- Mishra PK, Verma MK (2010) Energy spectra and fluxes for Rayleigh-Bénard convection. *Phys Rev E Stat Nonlin Soft Matter Phys* 81(5 Pt 2):056316.
- Yakhot V (1992) 4/5 Kolmogorov law for statistically stationary turbulence: Application to high-Rayleigh-number Bénard convection. *Phys Rev Lett* 69(5):769–771.
- Kumar A, Chatterjee AG, Verma MK (2014) Energy spectrum of buoyancy-driven turbulence. *Phys Rev E Stat Nonlin Soft Matter Phys* 90(2):023016.
- Ashurst WT, Kerstein AR, Kerr RM, Gibson CH (1987) Alignment of vorticity and scalar gradient with strain rate in simulated Navier-Stokes turbulence. *Phys Fluids* 30:2343–2353.
- Zeff BW, et al. (2003) Measuring intense rotation and dissipation in turbulent flows. *Nature* 421(6919):146–149.
- Lüthi B, Tsinober A, Kinzelbach W (2005) Lagrangian measurement of vorticity dynamics in turbulent flow. *J Fluid Mech* 528:87–118.
- Scheel JD, Schumacher J (2014) Local boundary layer scales in turbulent Rayleigh-Bénard convection. *J Fluid Mech* 758:344–373.
- Kerr RM (1996) Rayleigh number scaling in numerical convection. *J Fluid Mech* 310:139–179.
- Schumacher J, et al. (2014) Small-scale universality in fluid turbulence. *Proc Natl Acad Sci USA* 111(30):10961–10965.